Superconducting Phase Induced by a Local Structure Transition in Amorphous math xmlns="http://www.w3.org/1998/Math/MathML" display="inline">mrow>msub>mrow>mi>Sb/mi>/mrow>mrow>mn>2/mn>/mrow>/msub>msub>mrow>mi>Se/mi>/mrow>mrow>mn>3/mn>/mrow>/msub>/mrow>/math> under High Pressure

Kai Zhang, Ming Xu, Nana Li, Meng Xu, Qian Zhang, Eran Greenberg, Vitali B. Prakapenka, Yu-Sheng Chen, Matthias Wuttig, Ho-Kwang Mao, and Wenge Yang

Phys. Rev. Lett. **127**, 127002 — Published 15 September 2021

DOI: 10.1103/PhysRevLett.127.127002

Superconducting phase induced by a local structure transition in amorphous Sb_2Se_3 under high pressure

Kai Zhang[1, #], Ming Xu[2, #], Nana Li[1, #], Meng Xu[2], Qian Zhang[1], Eran Greenberg[3, †], Vitali B. Prakapenka[3], Yu-Sheng Chen[4], Matthias Wuttig[5], Ho-Kwang Mao[1], Wenge Yang[1, *]

[1]*Center for High Pressure Science and Technology Advanced Research (HPSTAR), Shanghai 201203, P. R. China*

[2]*Wuhan National Laboratory for Optoelectronics, School of Optical and Electronic Information, Huazhong University of Science and Technology, Wuhan 430074, China*

[3]*GSECARS, University of Chicago, Chicago, Illinois 60637, USA*

[4]*NSF's ChemMatCARS, University of Chicago, Chicago, Illinois 60637, USA*

[5]*Institute of Physics IA, RWTH Aachen University, 52074, Aachen, Germany*

Superconductivity and Anderson localization represent two extreme cases of electronic behavior in solids. Surprisingly, these two competing scenarios can occur in the same quantum system, e.g., in an amorphous superconductor. Although the disorder-driven quantum phase transition has attracted much attention, its structural origins remain elusive. Here, we discovered an unambiguous correlation between superconductivity and density in amorphous Sb_2Se_3 at high pressure. Superconductivity first emerges in the high-density amorphous (HDA) phase at about 24 GPa, where the density of glass unexpectedly exceeds its crystalline counterpart, and then shows an enhanced critical temperature when pressure induces crystallization at 51 GPa. *Ab initio* simulations reveal that the bcc-like local geometry motifs form in HDA phase, arising from distinct "metavalent bonds". Our results demonstrate that HDA phase is critical for the incipient superconductive behavior.

DOI:

PACS numbers:

The correlation between superconductivity and disorder has been an intriguing and challenging puzzle in condensed matter physics [1]. Based on BCS theory, superconductivity is dominated by the binding of electrons into Cooper pairs that form a macroscopic quantum coherent state [2]. In contrast, the disorder typically enhances the localization of electrons (Anderson localization) [3], leading to higher resistance in amorphous solids. For a weakly disordered system, superconductivity is insensitive to disorder, such as impurities [3]. Therefore, superconductivity can occur in many disordered systems, ranging from amorphous chalcogenides (e.g., phase change materials) [4,5], metallic glass [6], high entropy alloys [7], strong coupled amorphous materials [8], to nitride films [9], amorphous oxides films [10], and other amorphous alloy films [11]. The disorder can even enhance the superconductivity critical temperature in some specific systems, such as two-dimensional (2D) layer materials [12], and amorphous Bi film [13]. However, when disorder reaches a critical level that can induce the localization of the electron wavefunction, a quantum phase transition occurs, which is termed as a superconductor-insulator transition (SIT) [1,14]. A body of theoretical and experimental work has provided significant insights into the nature of the SIT, for example, the formation of superconducting islands at the insulating side of the SIT [15], and the preformed Cooper pairs in disordered superconductors well above the superconductivity critical temperature, T_c [10,16].

However, from a structural point of view, it is difficult to precisely define disorder in amorphous solids. Although superconductivity in disordered systems was first found in amorphous Bi films [13], its structural origin remains unknown [17]. To a large extent, this is ascribed to the complicated topological and chemical order in glass, and limitations of the experimental techniques accessible under extreme conditions [17]. A plausible picture has claimed that superconductivity in amorphous Bi results from its higher packing density than crystalline Bi but convincing experimental evidence is absent [18]. High pressure provides an effective route to tune the structural disorder and electron localization in amorphous solids [19-25], as demonstrated by the observation of superconductivity in As_2Te_3 glass [26], amorphous Ge [27], and Ge-Sb-Te phase-change materials [4,28] at high pressure. Yet, so far there is no consensus regarding the local atomic arrangement that facilitates the emergence of superconductivity.

Amorphous Sb_2Se_3 (a-Sb_2Se_3) provides a unique opportunity since it is rather stable against crystallization. The crystalline counterpart is characterized by strong spin-orbit coupling [29], and forms a topological insulator [30]. Crystalline Sb_2Se_3 transforms from a topologically trivial to a nontrivial state at 1 GPa [31] and displays superconductivity above 10 GPa [29]. This immediately raises two questions: do these electronic changes even occur in the amorphous state? How do changes in atomic arrangement affect the electronic properties of the amorphous state? In this work, we have performed a systematic study of the atomic arrangement and electronic properties of a-Sb_2Se_3 at high pressure, correlating its superconductivity to the density and revealing a unique bonding mechanism responsible for the formation of an amorphous superconductor.

Amorphous Sb_2Se_3 was prepared by the conventional thermal evaporation method [32]. The amorphous structure was measured using synchrotron high-pressure X-ray diffraction with a wavelength of 0.2952 Å. *In situ* high pressure was generated by a membrane diamond anvil cell (DAC) with a 100 µm culet size, using a Rhenium gasket, and silicon oil as pressure transmitting medium. A ruby ball and Au foil were used to calibrate the pressure. Low-temperature electrical resistance was measured in a CuBe alloy cell using a physical property measurement system (DynaCool, Quantum Design Inc.). The diamond culet size is 300 µm. The stainless steel was used as a gasket. A mixture of epoxy and powdered cubic boron nitride was used for electrical insulation. No pressure transmitting medium was used. Platinum foils with a thickness of 2 µm were used for the electrodes. The standard van der Pauw method was adopted to measure the resistance by four-probe configuration. Room temperature electrical resistance was measured using a stainless-steel DAC with a 250 µm culet size. The ab initio simulations were performed using the Vienna Ab initio Software Package. More detailed information about the experiment and simulation procedure is shown in the supplementary materials [33].

The electric transport measurement of a-Sb_2Se_3 at room temperature is shown in Fig. 1a upon compression up to 72.5 GPa and subsequent decompression. The resistivity drops by seven orders of magnitude between 0 and 20 GPa. Then, up to 57.2 GPa a much smaller resistivity decrease is found, followed by a small inflection at 57.2 GPa towards lower resistivity (The three-step transformation sequence for the electronic conductivity σ is shown in the inset as well). The electric transport properties were further measured at high pressure and low temperature (Fig. 1b-c). For pressure below 21.7 GPa, the resistance versus temperature curve R(T) shows the typical behavior of a semiconductor, i.e., a negative R-T coefficient. At higher pressure, the resistance displays a sharp decrease at low temperature. A more detailed measurement (run 2) confirmed that superconductivity appears at 23.9 GPa with a critical temperature of $T_c \sim 4.5$ K (Fig. 1c and S1a-c). Superconductivity is further verified by the suppression of the T_c with increasing magnetic field (Fig. 1e-f). Upon further compression, the T_c gradually increased to 6.5 K at 51 GPa and simultaneously showed another higher transition temperature at 7.5 K at 0 T (Fig. 1e). This generally implied the appearance of an additional superconducting phase with a higher transition temperature [4]. When increasing pressure to 60 GPa, only one single $T_c \sim 7.9$ K was found (Fig. 1f). During decompression, superconductivity can be maintained at a relatively higher $T_c \sim 10$ K until its disappearance at 25 GPa, at which double T_c transitions appear again (Fig. S1d). The detailed T_c is later shown in the superconducting phase diagram of Fig. 4b. We estimate the value of the upper critical magnetic field (H_{c2}, the magnetic field at which superconductivity disappears at zero temperature), using Werthamer-Helfand-Hohenberg formula [36] that has successfully predicted the upper critical magnetic field of amorphous superconductor [6],

$$H_{c2}^{\mathrm{WHH}}(0) = -0.693 T_c (dH_{c2}/dT)_{T=T_c}.$$

The estimated upper critical field value, $\mu_0 H_{c2}(0)$, is shown in Fig. 1d. The decompression process shows a higher $\mu_0 H_{c2}(0)$ than the compression process, which means superconductivity is more robust during decompression.

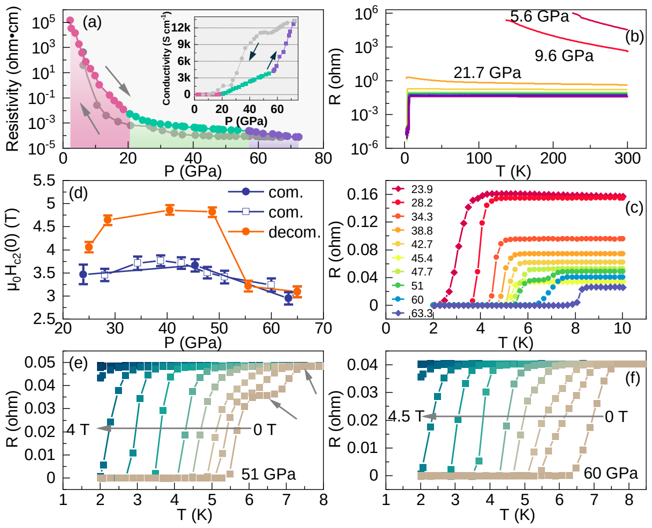

FIG. 1 Electric transport measurements of a-Sb_2Se_3 at high pressure. (a) Resistivity changes under compression and decompression at room temperature. The inset shows the change in the σ-P slope represented by pink, green, and purple colors, respectively. (b) Characterization of superconducting transition upon compression. (c) Detailed measurements near the superconducting transition temperature. The data at 23.9, 45.4, and 63.3 GPa are from run#2. (d) Superconducting upper critical field upon compression (blue) and decompression (orange). Open symbols are from run#1, solid symbols are from run#2. Magnetic field dependent R(T) of superconducting transition at 51 GPa (e) and 60 GPa (f).

In situ high-pressure synchrotron X-ray diffraction (XRD) was performed to reveal the structural origin of superconductivity (the original data are shown in Fig. S2a and S2b). Upon compression, the evident change is that a-Sb_2Se_3 experiences an amorphous to crystalline transition at 58.1 GPa. The crystalline phase persists to the highest pressure in this study, 78.2 GPa, which is verified as a bcc structure by structural analysis (Fig. S2d). During decompression, bcc-Sb_2Se_3 returns to the amorphous phase at about 24 GPa and finally recovers to the initial a-Sb_2Se_3 structure. The reversible pressure-induced crystallization is not very common in disordered materials, but such a transition is frequently seen in amorphous chalcogenides, probably due to the large flexibility in terms of local structure and chemical bonds [37].

Furthermore, we extracted the structure factors of a-Sb_2Se_3, $S(q)$, and the pair distribution functions, $g(r)$, to correlate the local atomic arrangement with superconductivity (Fig. 2a and b). Surprisingly, there are two regimes for the shift of the principal peak of $S(q)$ located near 2.2 Å^{-1} as shown in Fig. 2c. With increasing pressure, the peak shift proceeds at a relatively faster pace over the low-pressure range of 0.6-15.7 GPa at approximately 0.021 Å^{-1}/GPa, but at a slower pace of 0.0048 Å^{-1}/GPa above 15.7 GPa. In the $g(r)$ plot (Fig. 2d), two distinct regimes of peak shift for the nearest neighbor atomic distance, r_1, can be seen. Below 15.7 GPa, r_1 enlarges unexpectedly to a longer distance followed by a gradual compression at higher pressure (also indicated as the orange triangle in Fig. 2e). It is reported that the crystalline Sb_2Se_3 undergoes a structural phase transition from the orthorhombic *P*nma phase to the bcc *I*m-3m phase at 51 GPa [38]. Therefore, we compared the local structure evolution between amorphous, *P*nma, and bcc Sb_2Se_3, by the reduced pair distribution function G(r) as detailed in Fig. S3. The resulting r_1 of $G(r)$ is plotted in Fig. 2e, which clearly demonstrates that r_1 of amorphous phase gradually deviates from the *P*nma structure (low-pressure crystalline phase) toward bcc-like one (high-pressure crystalline phase).

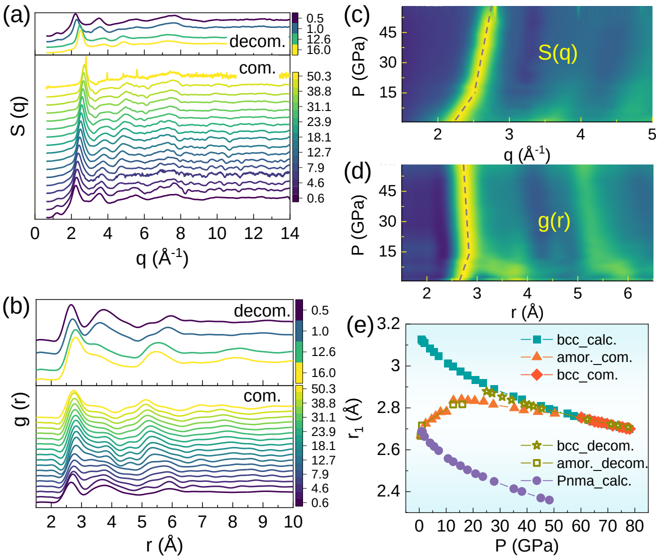

FIG. 2 Structure evolution of a-Sb_2Se_3 under high pressure. (a) $S(q)$ and (b) $g(r)$ under compression and decompression. (c, d) The corresponding principal peak positions shift with pressure, showing a slope change at around 15.7 GPa. (e) Comparison of pressure dependence of r_1 for amorphous, *P*nma (low-pressure crystalline structure), and bcc phase (high-pressure crystalline structure). Error bar of r_1 is smaller than the symbol size. All pressure values are in GPa.

To corroborate the atomic structure changes described above, the simulated structure evolutions with applied pressure are performed as shown in Fig. 3. At low pressure, the first and second peaks of $g(r)$ are recognizable (Fig. 3a). With increasing pressure, the first peak gradually shifts to a larger distance at 20 GPa (see the vertical dashed line in Fig. 3a) and subsequently contracted, which is consistent with experimental $g(r)$. The second peak gradually merges with the first peak and evolves into a shoulder-like feature, finally becoming indistinguishable at 50 GPa. In Fig. S4a, the partial $g(r)$ indicates that with increasing pressure the Se-Se correlation distance at 3.85 Å abruptly diminishes, in contrast to a small change in the Sb-Sb distance. Therefore, the expansion of r_1 at low pressure is mainly ascribed to the Se atoms squeezed into the first neighbor shell.

It is noteworthy that the angle distribution function (ADF) shows the appearance of a 60º bond angle starting at 16 GPa (red arrow in Fig. 3b), which demonstrates that a short-range order (SRO) change is triggered. After 20 GPa, ADF transforms into a distinctly different profile. More specifically, the ADF changes around the Se atoms are more apparent than those around the Sb atoms (Fig. S4b), which is compatible with the large atom motion of Se in partial g(r) as mentioned above. This structural change is also manifested by the increased coordination number (CN) at applied pressure with a slight transition at 16 GPa, which is consistent with the experimental CN change (Fig. 3c). As a result, the local geometry units transform from 6, 7, 8-member rings to 3-member rings at 20 GPa (Fig. 3d).

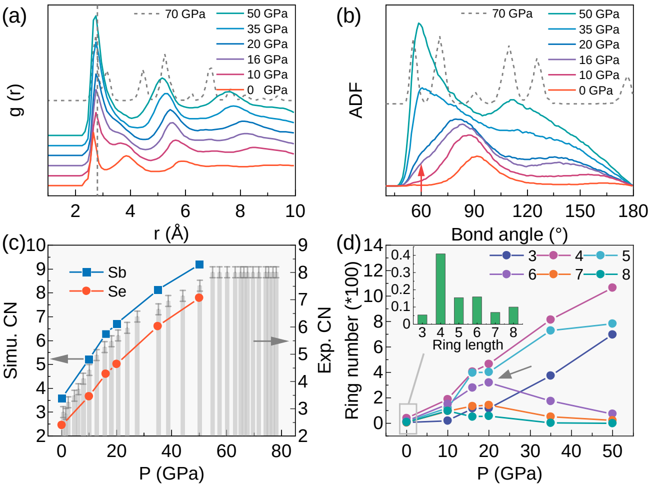

FIG. 3 Simulated structural features of a-Sb_2Se_3 upon compression. (a) $g(r)$, the vertical dashed line marks the largest position of the first peak. (b) Angle distribution function, showing the appearance of the 60° bond angle starting at 16 GPa. (c) Simulated partial coordination number around Sb and Se atoms indicates a subtle but definite transition at 16 GPa, which is in accord with experimental CN (gray bars). (d) The statistic distribution of ring length, showing a local structural transition from long to short member rings at 20 GPa. For clarity, the inset shows the distribution of ring length at 0 GPa with 4-member ring as the main structural unit. The vertical axis value is the relative ratio of various local structure units.

Taken together, the appearance of superconductivity is clearly related to the intermediate amorphous phase. To correlate them, a diagram of the volume and superconductivity versus applied pressure is shown in Fig. 4. The initial density of a-Sb_2Se_3 is 16% smaller than that of the crystalline phase at ambient pressure (Fig. 4a). This is attributed to an open network glass structure [19,39] as indicated by the prepeak in S(q) (Fig. 2a) and the first sharp diffraction peak (FSDP) at ~ 1.2 Å^{-1} (Fig. S2c), which generally signifies the prevalence of medium-range order (MRO) in glass [40]. Upon compression, the density of a-Sb_2Se_3 quickly increases due to the collapse of network structure as indicated by the sharply diminished FSDP. More surprisingly, amorphous density even surpasses the crystalline phase at 16 GPa, which is attributed to the formation of more compact local structure as demonstrated by the transition of the bond angle, r_1, and CN. Although crystalline Sb_2Se_3 only shows the orthorhombic structure in the same pressure range [38], the present results suggest two different structural motifs in a-Sb_2Se_3 at low and high pressures, accordingly, dictating different compression mechanisms. Based on density crossover and SRO changes, we thus divide the amorphous range into low-density amorphous (LDA) and high-density amorphous (HDA) regions with the critical point at around 20 GPa, which are governed by MRO and SRO changes, respectively.

A T_c-P diagram is summarized in Fig. 4(b) by plotting the T_c versus pressure, considering both a-Sb_2Se_3 and bcc-Sb_2Se_3. The T_c gradually increases with pressure because the density and SRO of HDA phase gradually approach those of the bcc phase [Fig. 4(b)]. When reaching the phase transition point at around 50 GPa, the local structure of HDA phase, such as $g(r)$ and ADF, has highly resembled the bcc phase (70 GPa) (dash line in Fig. 3 a and b), therefore, a-Sb_2Se_3 shows a clear T_c upturn that is suggested by the increased T_c slope with pressure (Fig. 4b). Superconductivity persists up to the highest pressure studied, 65 GPa. During decompression, T_c increases slightly and saturates at 25 GPa. It disappears suddenly when the high-pressure bcc phase collapses into the LDA phase. It should be noted that there is a small pressure difference in HDA-bcc transition for XRD and room/low temperature resistance measurements, which is mainly attributed to non-hydrostatic conditions that cause stress inhomogeneity.

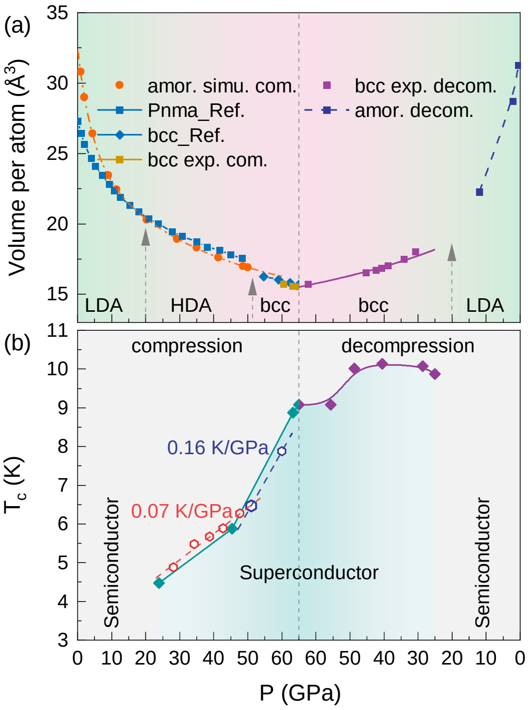

FIG. 4 Density dependence of superconductivity at high pressure. (a) Equation of state of a-Sb_2Se_3 that experiences an LDA-HDA-bcc phase transition during compression and an abrupt bcc-LDA transition upon decompression. Volume data of *P*nma and bcc Sb_2Se_3 are taken from Ref. [38]. (b) Superconducting phase diagram, showing superconductivity starting at 23.9 GPa in HDA and a noticeable T_c upturn at 50 GPa that corresponds to the appearance of the bcc phase. Superconductivity is preserved down to 25 GPa upon decompression when Sb_2Se_3 returns to an LDA. The open and solid symbols are for two independent compression runs.

The atomic arrangement in solids essentially depends on the chemical bonds between adjacent atoms, which can be represented by a competition between electron localization (ionic or covalent bonding) and electron delocalization (metallic bonding) [39,41-43]. Unlike the abrupt phase transition in amorphous Si or Ge [20,44,45], polyamorphism in chalcogenide glass leads to a relatively continuous change, which is traditionally attributed to a semiconductor-metal transition [4]. However, the anomalous intermediate behavior in the structural and electronic aspects observed in the HDA Sb_2Se_3 cannot be explained by covalent or metallic bonding alone. In terms of the conductivity (inset in Fig. 1a), HDA Sb_2Se_3 falls within a narrow linear range from 190 to 4000 S/cm, resembling the value of incipient metals [46,47]. Interestingly, this special class of materials is recently relevant for a variety of applications, including phase change materials, thermoelectrics, topological insulators, and photonic devices [48]. It is attributed to a unique bonding mechanism, named metavalent bonding (MVB) [47,49], which is closely related to local structure distortion and electron localization strength [42,50]. Indeed, similar resistivity values have been observed for crystalline sesqui-chalcogenides such as Bi_2Se_3, Bi_2Te_3, and Sb_2Te_3 which present MVB, while crystalline Sb_2Se_3 without MVB shows a much higher resistivity [50,51].

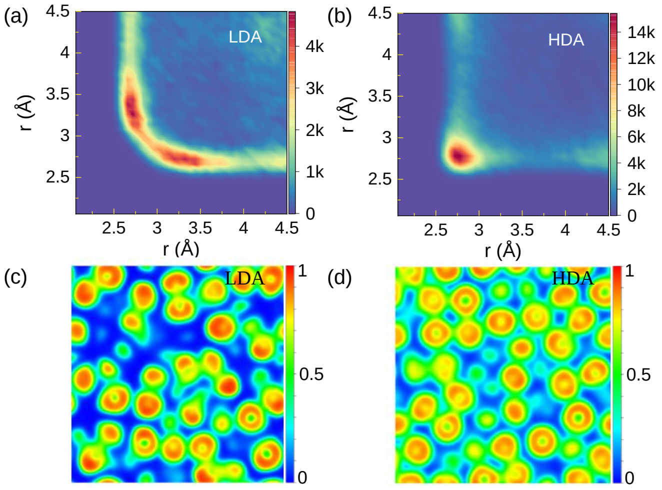

FIG. 5 Characterization of PLD (a, b) depicted by the distribution of long- and short-bonds and ELF (c, d) in LDA (0 GPa) and HDA (35 GPa) phase, respectively. The ELF value of 1 represents perfect electronic localization (red), 0.5 represents perfect electronic delocalization (green), and 0 represents void regions (blue).

In semiconducting materials with a narrow bandgap, Peierls-like distortion (PLD) is prevalent, to minimize the electronic energy and, thus, stabilize the structure [52,53]. PLD describes the formation of the long- and short-bond around a centered atom where the statistic distribution of bond pairs is limited to an angle close to 180°. Typically, PLD is extremely large in an amorphous state compared to its crystalline counterpart. Therefore, LDA Sb_2Se_3 is a covalently-bonded semiconducting material that shows pronounced PLD (Fig. 5a). For HDA, the local atomic environment gradually approaches the cubic structure upon compression as evidenced by the decreased PLD (Fig. 5b), which is characterized by MVB. This is consistent with MVB systems in which small PLD are frequently encountered [47]. Electronic instability is concomitant with PLD due to the repartitioning of the electrons between long- and short bonds.

The electron localization function (ELF) can give a quantitative description of the chemical bonding [54,55]. Apparently, when applying high pressure on a-Sb_2Se_3, highly localized electrons in LDA phase transform toward a more delocalized state (more green areas in HDA phase, Fig. 5c-d).

In summary, combining the *in situ* high-pressure X-ray diffraction and electric transport measurement results, we establish the superconducting phase diagram of a-Sb_2Se_3 up to 65 GPa, which was confirmed by *ab initio* simulations. a-Sb_2Se_3 shows a highly flexible network structure and resistivity change at high pressure, governed by distinct structural rearrangement on different length scales. HDA phase, featured by metavalent bonding, plays a pivotal role in the delocalization of electrons and the occurrence of superconductivity in the amorphous state. Interestingly, the disorder in materials with similar properties such as disordered crystalline Sb_2Te_3, $SnSb_2Te_4$, and $GeSb_2Te_4$ has recently been found to lead to Anderson localization [43,56,57]. The results presented here provide a structural basis for the incipient structure of pressure-induced superconductivity in amorphous solids.

This work was supported by the National Nature Science Foundation of China under Grants No. 11804010, U1930401, 51527801, China Postdoctoral Science Fund (Grant No. 2016M600909), and China Scholarship Council. M.W. acknowledges support by the Deutsche Forschungsgemeinschaft (SFB 817). The beamline 13-ID-D (GeoSoiEnviroCARS) was supported by the National Science Foundation (NSF)-Earth Sciences (EAR-1128799) and Department of Energy (DOE)-GeoSciences (DE-FG02-94ER14466). APS is supported by DOE-BES, under Contract No. DE-AC02-06CH11357.

# Kai Zhang, Ming Xu, and Nana Li contributed equally to this work.

† Present address: Applied Physics Division, Soreq NRC, Yavne, 81800, Israel

*Corresponding author: yangwg@hpstar.ac.cn (Wenge Yang)

[1] B. Sacépé, M. Feigel'man, and T. M. Klapwijk, Nature Physics **16**, 734 (2020).

[2] J. Bardeen, L. N. Cooper, and J. R. Schrieffer, Physical review **108**, 1175 (1957).

[3] P. W. Anderson, Journal of Physics and Chemistry of Solids **11**, 26 (1959).

[4] E. Greenberg *et al.*, Physical Review B **95**, 064514 (2017).

[5] N. F. Mott, Journal of Non-Crystalline Solids **164-166**, 1177 (1993).

[6] N. Toyota, A. Inoue, T. Fukase, and T. Masumoto, Journal of Low Temperature Physics **55**, 393 (1984).

[7] J. Guo *et al.*, Proceedings of the National Academy of Sciences of the United States of America **114**, 13144 (2017).

[8] M. Baggioli, C. Setty, and A. Zaccone, Physical Review B **101**, 214502 (2020).

[9] B. Sacepe, C. Chapelier, T. I. Baturina, V. M. Vinokur, M. R. Baklanov, and M. Sanquer, Phys Rev Lett **101**, 157006 (2008).

[10] T. Dubouchet, B. Sacépé, J. Seidemann, D. Shahar, M. Sanquer, and C. Chapelier, Nature Physics **15**, 233 (2019).

[11] J. M. Graybeal and M. R. Beasley, Physical Review B **29**, 4167 (1984).

[12] K. Zhao *et al.*, Nature Physics **15**, 904 (2019).

[13] W. Buckel and R. Hilsch, Zeitschrift für Physik **138**, 109 (1954).

[14] M. Ma and P. A. Lee, Physical Review B **32**, 5658 (1985).

[15] Y. Dubi, Y. Meir, and Y. Avishai, Nature **449**, 876 (2007).

[16] B. Sacépé, T. Dubouchet, C. Chapelier, M. Sanquer, M. Ovadia, D. Shahar, M. Feigel'man, and L. Ioffe, Nature Physics **7**, 239 (2011).

[17] Z. Mata-Pinzon, A. A. Valladares, R. M. Valladares, and A. Valladares, PLoS One **11**, e0147645 (2016).

[18] G. Bergmann, Physics Reports **27**, 159 (1976).

[19] M. Xu, Y. Q. Cheng, L. Wang, H. W. Sheng, Y. Meng, W. G. Yang, X. D. Han, and E. Ma, Proceedings of the National Academy of Sciences of the United States of America **109**, E1055 (2012).

[20] P. F. McMillan, M. Wilson, D. Daisenberger, and D. Machon, Nature materials **4**, 680 (2005).

[21] H. W. Sheng, H. Z. Liu, Y. Q. Cheng, J. Wen, P. L. Lee, W. K. Luo, S. D. Shastri, and E. Ma, Nature materials **6**, 192 (2007).

[22] J. P. Itie, A. Polian, G. Calas, J. Petiau, A. Fontaine, and H. Tolentino, Physical Review Letters **63**, 398 (1989).

[23] Z. Sun, J. Zhou, Y. Pan, Z. Song, H. K. Mao, and R. Ahuja, Proceedings of the National Academy of Sciences of the United States of America **108**, 10410 (2011).

[24] A. Polian, M. Grimsditch, and E. Philippot, Physical Review Letters **71**, 3143 (1993).

[25] X.-B. Li, X. Q. Liu, X. Liu, D. Han, Z. Zhang, X. D. Han, H.-B. Sun, and S. B. Zhang, Physical Review Letters **107**, 015501 (2011).

[26] N. Sakai and H. Fritzsche, Physical Review B **15**, 973 (1977).

[27] O. I. Barkalov, V. G. Tissen, P. F. McMillan, M. Wilson, A. Sella, and M. V. Nefedova, Physical Review B **82**, 020507 (2010).

[28] B. Hen *et al.*, Physical Review B **97**, 024513 (2018).

[29] P. P. Kong *et al.*, Scientific reports **4**, 6679 (2014).

[30] A. Bera, K. Pal, D. V. S. Muthu, S. Sen, P. Guptasarma, U. V. Waghmare, and A. K. Sood, Physical Review Letters **110**, 107401 (2013).

[31] W. Li, X.-Y. Wei, J.-X. Zhu, C. Ting, and Y. Chen, Physical Review B **89**, 035101 (2014).

[32] K. Zhang, Y. Li, Q. Huang, B. Wang, X. Zheng, Y. Ren, and W. Yang, The journal of physical chemistry. B **121**, 8188 (2017).

[33] See Supplemental Material [……] for more detailed information about the experiment, simulation procedure, and data processing, which includes Refs. [34-35].

[34] C. Prescher and V. B. Prakapenka, High Pressure Research **35**, 223 (2015).

[35] C. Farrow, P. Juhas, J. Liu, D. Bryndin, E. Božin, J. Bloch, T. Proffen, and S. Billinge, Journal of Physics: Condensed Matter **19**, 335219 (2007).

[36] N. R. Werthamer, E. Helfand, and P. C. Hohenberg, Physical Review **147**, 295 (1966).

[37] G. Parthasarathy and E. Gopal, Bulletin of Materials Science **7**, 271 (1985).

[38] I. Efthimiopoulos, J. Zhang, M. Kucway, C. Park, R. C. Ewing, and Y. Wang, Scientific reports **3**, 2665 (2013).

[39] W. Zhang, A. Thiess, P. Zalden, R. Zeller, P. H. Dederichs, J. Y. Raty, M. Wuttig, S. Blugel, and R. Mazzarello, Nature materials **11**, 952 (2012).

[40] S. R. Elliott, Nature **354**, 445 (1991).

[41] C. Bellin, A. Pawbake, L. Paulatto, K. Béneut, J. Biscaras, C. Narayana, A. Polian, D. J. Late, and A. Shukla, Physical Review Letters **125**, 145301 (2020).

[42] A. Pawbake, C. Bellin, L. Paulatto, K. Béneut, J. Biscaras, C. Narayana, D. J. Late, and A. Shukla, Physical Review Letters **122**, 145701 (2019).

[43] T. Siegrist, P. Jost, H. Volker, M. Woda, P. Merkelbach, C. Schlockermann, and M. Wuttig, Nature materials **10**, 202 (2011).

[44] V. L. Deringer, N. Bernstein, G. Csányi, C. Ben Mahmoud, M. Ceriotti, M. Wilson, D. A. Drabold, and S. R. Elliott, Nature **589**, 59 (2021).

[45] S. K. Deb, M. Wilding, M. Somayazulu, and P. F. McMillan, Nature **414**, 528 (2001).

[46] J. Mooij, physica status solidi (a) **17**, 521 (1973).

[47] M. Wuttig, V. L. Deringer, X. Gonze, C. Bichara, and J. Y. Raty, Adv Mater **30**, e1803777 (2018).

[48] B. J. Kooi and M. Wuttig, Adv Mater **32**, e1908302 (2020).

[49] J. Y. Raty, M. Schumacher, P. Golub, V. L. Deringer, C. Gatti, and M. Wuttig, Adv Mater **31**, e1806280 (2019).

[50] Y. Cheng, S. Wahl, and M. Wuttig, physica status solidi (RRL) – Rapid Research Letters **15**, 2000482 (2020).

[51] Y. Cheng *et al.*, Adv Mater **31**, e1904316 (2019).

[52] Z. Sun, J. Zhou, H.-K. Mao, and R. Ahuja, Proceedings of the National Academy of Sciences **109**, 5948 (2012).

[53] M. Wuttig, D. Lusebrink, D. Wamwangi, W. Welnic, M. Gillessen, and R. Dronskowski, Nature materials **6**, 122 (2007).

[54] A. Savin, R. Nesper, S. Wengert, and T. F. Fässler, Angewandte Chemie International Edition in English **36**, 1808 (1997).

[55] B. Silvi and A. Savin, Nature **371**, 683 (1994).

[56] I. Korzhovska, H. Deng, L. Zhao, Y. Deshko, Z. Chen, M. Konczykowski, S. Zhao, S. Raoux, and L. Krusin-Elbaum, npj Quantum Materials **5**, 39 (2020).

[57] J. Reindl, H. Volker, N. P. Breznay, and M. Wuttig, npj Quantum Materials **4**, 57 (2019).